

HIGH-ORDER ACCURATE EMBEDDED-BOUNDARY DISCONTINUOUS GALERKIN METHODS FOR INVISCID GAS DYNAMICS

Vincenzo Gulizzi^{1,2}

¹Department of Engineering, Università degli Studi di Palermo, Palermo, 90128, Italy

²Center for Computational Sciences and Engineering, Lawrence Berkeley National Laboratory, Berkeley, CA 94720, USA

Abstract

This work presents a computational framework for solving the equations of inviscid gas dynamics over embedded geometries based on the discontinuous Galerkin (DG) method. The novelty of the framework is the ability to achieve high-order accuracy in the regions of smooth flow and to handle the presence of solution discontinuities via suitably-introduced damping terms, which allow controlling spurious oscillations that are typical of high-order methods for first-order hyperbolic PDEs. The framework employs block-structured Cartesian grids where a level set function defines implicitly the considered geometry. The domain is partitioned by intersecting the grid and the level set function, such that the resulting mesh consists of a collection of standard d -dimensional rectangular cells and a relatively smaller number of irregular cut cells in proximity of the boundary of the embedded geometry, with a simple cell merging strategy handling the presence of overly small cut cells. The DG formulation is used to discretize the governing equations in space and to introduce the damping terms. Runge-Kutta algorithms are then employed to integrate the resulting semi-discrete equations in time. Numerical tests are presented to show the high-order accuracy and the shock-capturing capabilities of the proposed approach.

Keywords: Embedded boundaries; High-order accuracy; Discontinuous Galerkin methods; Gas dynamics

1. Introduction

In computational sciences, embedded-boundary (EB) methods, which include cut-cell, immersed-boundary and fictitious-domain methods, denote a class of numerical techniques where the domain of analysis is represented as a separate entity in a background grid, and the boundaries and interfaces of one or multiple considered phases do not need to conform to the boundaries of the grid's cells. With respect to alternative domain-partition strategies, such as unstructured body-fitted meshes, EB methods allow simpler approaches to mesh generation, data storage and adaptive mesh refinement, and benefit from the high regularity of the mesh elements in most of the domain [1]. Nevertheless, to resolve the boundaries and interfaces of the embedded geometries, special treatments are required, especially when high-order accuracy is desired.

In general, EB methods may be designed following two different approaches, namely diffused-interface methods, see e.g. [2, 3], and sharp-interface methods, see e.g. [4, 5, 6, 7]. In diffused-interface methods, the transition between the different phases is assumed to occur smoothly through a finite-thickness region; these methods allow the use of purely Cartesian meshes but typically require a highly refined mesh in the transition region. On the other hand, in sharp-interface methods, the embedded boundaries and interfaces are represented in sharp sense as lower-dimensional curves (in 2D) or surfaces (in 3D); these methods allow retaining the information of the geometry but introduce the so-called *small cells*, i.e. those cells that are cut by the embedded geometry and have overly small volume fractions. To remedy the small-cell problem, several techniques have been proposed in the literature, such as the cell-merging strategy [8, 9], the flux-redistribution method [10] and the state-redistribution method [11], among others. These methods have been successfully employed in

combination with Finite Volume (FV) schemes, which are generally second-order accurate in space. However, if higher order accuracy is desired, their development become more convoluted.

As an alternative to FV schemes, discontinuous Galerkin (DG) methods [12] have proved to be powerful and versatile techniques, that offer high-order accuracy with compact stencil and generally-shaped mesh elements, block-structured mass matrices, and a natural way to handle hp adaptive mesh refinement, which are highly desirable features in high-performance computing applications. In the context of compressible flow, various DG approaches have successfully been proposed in the literature, typically in combination with the cell-merging strategy, see for example [4, 13, 14, 15, 7]. However, in these studies, one of the long-standing problem is the treatment of spurious oscillations of the DG solution in the presence of discontinuities, which may lead to numerical instabilities and blowup. In this work, following the approach proposed in Refs.[17, 18] for oscillation-free DG methods defined over triangular meshes, a novel oscillation-free DG formulation for inviscid gas dynamics over embedded geometries is presented.

The paper is organized as follows: Sec.(2). introduces the governing equations that are considered to model inviscid gas dynamics problems; Sec.(3). describes the geometry representation and mesh generation strategy; Sec.(4). presents the proposed oscillation-free embedded-boundary DG formulation; Sec.(5). describes the results of the performed numerical tests on two sets of tests aimed at verifying the high-order accuracy as well as the shock-capturing capabilities of the proposed formulation; Sec.(6). concludes the paper.

2. Governing equations

We consider a domain $\mathcal{D} \subset \mathbb{R}^d$ and a time interval $\mathcal{T} \equiv [0, T]$, where d is the spatial dimension and T is the final time of the analysis. We also consider a hyperbolic set of first-order conservation laws of the form

$$\frac{\partial \mathbf{U}}{\partial t} + \frac{\partial \mathbf{F}_k}{\partial x_k} = \mathbf{0}, \quad \text{for } (t, \mathbf{x}) \in \mathcal{D} \times \mathcal{T}, \quad (1)$$

where t denotes the time, x_k denotes the k -th component of the d -dimensional space location vector $\mathbf{x} \equiv (x_1, \dots, x_d)$, \mathbf{U} is the N_U -dimensional vector of the conserved variables, $\mathbf{F}_k = \mathbf{F}_k(\mathbf{U})$ is the N_U -dimensional vector of the fluxes along the k direction, and N_U denotes the number of conserved variables. In Eq.(1) and in the remainder of this paper, the subscript k takes value in $\{1, \dots, d\}$ and implies summation when repeated.

To model inviscid gas dynamics in \mathbb{R}^d , the number of conserved variables is $N_U \equiv d + 2$, and \mathbf{U} and \mathbf{F}_k are defined as follows

$$\mathbf{U} \equiv \begin{pmatrix} \rho \\ \rho \mathbf{v} \\ \rho E \end{pmatrix} \quad \text{and} \quad \mathbf{F}_k \equiv \begin{pmatrix} \rho v_k \\ \rho v_k \mathbf{v} + p \delta_k \\ (\rho E + p)v_k \end{pmatrix}, \quad (2)$$

where ρ is the density, $\mathbf{v} \equiv (v_1, \dots, v_d)^\top$ is the vector of the velocity components, p is the pressure and E is the total energy. The governing equations are closed upon considering an ideal gas characterized by the ratio γ of specific heats such that

$$p = (\gamma - 1) \left(\rho E - \frac{1}{2} \rho v_k v_k \right). \quad (3)$$

3. Geometry representation and mesh generation

The governing equations given in (1) are solved over a mesh of the domain \mathcal{D} . In this work, the implicitly-defined mesh technique [5, 6, 7, 16] is employed; its main steps are as follows:

- (i) The domain \mathcal{D} is enclosed within a background rectangle \mathcal{R} , where it is implicitly defined by a level set function $\varphi : \mathcal{R} \rightarrow \mathbb{R}$ as $\mathcal{D} \equiv \{\mathbf{x} \in \mathcal{R} : \varphi(\mathbf{x}) < 0\}$;
- (ii) The rectangle is partitioned via an easy-to-generate background grid $G^h \equiv \bigcup_i \mathcal{C}^i$, where h denotes a characteristic mesh size of the grid and \mathcal{C}^i is a generic d -dimensional rectangular cell whose location inside the grid is identified the d -tuple $\mathbf{i} \equiv (i_1, \dots, i_d)$;

- (iii) The cells are characterized by their volume fraction and those cells having an overly small volume fraction are suitably merged with their neighbors according to the procedure described in Refs.[7, 16];
- (iv) The mesh elements are eventually obtained by intersecting the merged and non-merged cells with the domain \mathcal{D} .

The resulting mesh of the domain is denoted by $\mathcal{D}^h \equiv \bigcup \mathcal{D}^e$, where \mathcal{D}^e is a generic mesh element. The meshing procedure is illustrated in Fig.(1): Fig.(1a) shows a two-dimensional domain embedded in a 4×4 background grid where $\mathcal{B} \equiv \{x \in \partial \mathcal{R} : \varphi(x) < 0\}$ and $\mathcal{L} \equiv \{x \in \mathcal{R} : \varphi(x) = 0\}$; Fig.(1b) shows the corresponding classification of the grid's cells based on their volume fraction; Fig.(1c) shows the resulting mesh and highlights a generic e -th element \mathcal{D}^e along with the associated outer boundary \mathcal{B}^e , outer unit normal $\mathbf{n}^e \equiv (n_1^e, \dots, n_d^e)$ and the internal boundary $\mathcal{I}^{e,e'}$ that the element shares with its neighbor $\mathcal{D}^{e'}$. The interested reader is referred to Refs.[5, 6, 7, 16] for a detailed description of the present meshing technique.

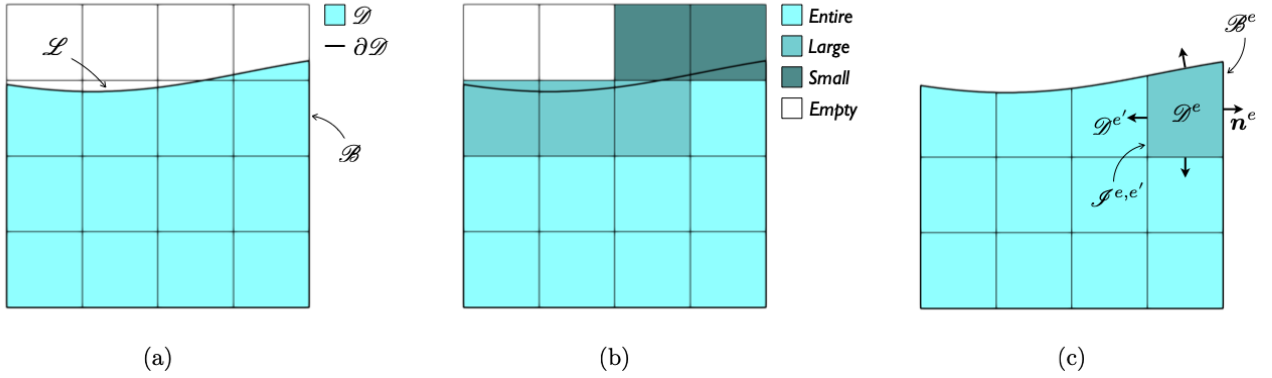


Figure 1 – (a) Sample two-dimensional domain \mathcal{D} embedded in a 4×4 background grid. (b) Cell classification based on their volume fraction. (c) Resulting implicitly-defined mesh.

4. Discontinuous Galerkin formulation

Once the mesh \mathcal{D}^h is introduced, the governing equations (1) are numerically solved over \mathcal{D}^h by using the Runge-Kutta (RK) discontinuous Galerkin approach developed by Cockburn and coworkers, see e.g. [12], whereby the DG method is utilized to discretize the spatial derivatives and the RK method is subsequently employed to advance the resulting semi-discrete equations in time.

In particular, let V^h be the space of discontinuous polynomial basis functions defined over \mathcal{D}^h as

$$V^h \equiv \{v : \mathcal{D}^h \rightarrow \mathbb{R} \mid v|_{\mathcal{D}^e} \in P_p^h(\mathcal{D}^e), \forall e = 1, \dots, N_e\}, \quad (4)$$

where P_p^h denotes the space of tensor-product polynomials of degree at most p defined for the element \mathcal{D}^e . Accordingly, the space of discontinuous N -dimensional polynomial vector fields is defined as $V^{hN} \equiv (V^h)^N$. Then, the DG formulation associated with the considered set of governing equations is derived from multiplying Eq.(1) by the test functions $\mathbf{V} \in V^{hN_U}$, integrating over a generic element \mathcal{D}^e and performing integration by parts, to obtain:

$$\int_{\mathcal{D}^e} \mathbf{V}^\top \frac{\partial \mathbf{U}^e}{\partial t} dV = \int_{\mathcal{D}^e} \frac{\partial \mathbf{V}^\top}{\partial x_k} \mathbf{F}_k^e dV - \int_{\partial \mathcal{D}^e} \mathbf{V}^\top \widehat{\mathbf{F}}_n dS, \quad \forall \mathbf{V} \in V^{hN_U}. \quad (5)$$

In Eq.(5), \mathbf{U}^e denotes the approximation of the vector \mathbf{U} of conserved variables over \mathcal{D}^e , \mathbf{F}_k^e denotes the fluxes evaluated using \mathbf{U}^e , i.e. $\mathbf{F}_k^e \equiv \mathbf{F}_k(\mathbf{U}^e)$, and $\widehat{\mathbf{F}}_n$ denotes the so-called numerical flux, which is a function of \mathbf{U}^e and the boundary conditions at \mathcal{B}^e , or a function of \mathbf{U}^e and $\mathbf{U}^{e'}$ at $\mathcal{I}^{e,e'}$. It is worth noting that $\widehat{\mathbf{F}}_n$ is the only terms responsible for linking neighboring mesh elements.

It is well known that Eq.(5) allows obtaining a high-order solution of the governing equations when the solution is smooth but leads to spurious oscillations in presence of discontinuities. As a consequence,

Eq.(5) may not be straightforwardly employed for modelling certain classes of non-linear first-order hyperbolic PDEs, such as those of inviscid gas dynamics, which may develop discontinuities even for smooth initial and boundary conditions. Here, following the approach recently proposed in Refs.[17, 18] for triangular meshes, the weak form given in Eq.(5) is suitably modified to read

$$\int_{\mathcal{D}^e} \mathbf{V}^\top \frac{\partial \mathbf{U}^e}{\partial t} dV = \int_{\mathcal{D}^e} \frac{\partial \mathbf{V}^\top}{\partial x_k} \mathbf{F}_k^e dV - \int_{\partial \mathcal{D}^e} \mathbf{V}^\top \widehat{\mathbf{F}}_n dS - \sum_{q=0}^p \frac{\sigma_q^e}{h} \int_{\mathcal{D}^e} \mathbf{V}^\top (\mathbf{U}^e - \mathbb{P}_q^h(\mathbf{U}^e)) dV, \quad \forall \mathbf{V} \in \mathbf{V}^{hN_U}, \quad (6)$$

where $\mathbb{P}_q^h(\mathbf{U})$ is defined using the standard L_2 projection of a vector function \mathbf{U} such that

$$\int_{\mathcal{D}^e} \mathbf{V}^\top (\mathbf{U} - \mathbb{P}_q^h(\mathbf{U})) dV = 0, \quad \forall \mathbf{V} \in \mathbf{P}_q^h(\mathcal{D}^e), \quad (7)$$

and $\mathbb{P}_{-1}^h(\mathbf{U}) \equiv \mathbb{P}_0^h(\mathbf{U})$. In Eq.(6), the terms σ_q^e are damping factors, which are defined here as follows

$$\sigma_q^e \equiv \frac{2(2q+1)}{2p-1} \frac{h^q}{q!} \max_s \left(\frac{1}{|\mathcal{I}^e|} \sum_{|\alpha|=q} \sum_{e'} \int_{\mathcal{I}^{e,e'}} (\partial^\alpha C^e - \partial^\alpha C^{e'})^2 dS \right)^{1/2}. \quad (8)$$

In Eq.(8), $|\mathcal{I}^e|$ denotes the measure of the internal boundaries of the e -th elements, i.e. $\mathcal{I}^e \equiv \bigcup_{e'} \mathcal{I}^{e,e'}$, $|\alpha| \equiv \alpha_1 + \dots + \alpha_d$, $\partial^\alpha \bullet$ is defined as

$$\partial^{\alpha \bullet} \equiv \frac{\partial^{|\alpha|} \bullet}{\partial^{\alpha_1} x_1 \dots \partial^{\alpha_d} x_d}, \quad (9)$$

and $\partial^\alpha C$ is the derivative of the vector of the characteristic variables obtained as

$$\partial^\alpha C \equiv \mathbf{R}^{-1} \partial^\alpha \mathbf{U}, \quad (10)$$

where \mathbf{R} is the matrix of the characteristic decomposition

$$n_k \mathbf{F}_k(\bar{\mathbf{U}}) \equiv \mathbf{R} \mathbf{\Lambda} \mathbf{R}^{-1} \quad (11)$$

and $\bar{\mathbf{U}}$ is the Roe average at the element interface. The expression given in Eq.(8) is introduced such that the terms σ_q^e are small in regions of smooth flow and large in proximity of the discontinuity. Upon letting \mathbf{V} range over the test functions and expressing \mathbf{U}^e in terms of polynomial basis functions multiplied by time-dependent coefficients, i.e. $\mathbf{U}^e(t, \mathbf{x}) = \mathbb{B}^e(\mathbf{x}) \mathbb{X}^e(t)$, it is possible to obtain the following semi-discrete form

$$\mathbb{M}^e \dot{\mathbb{X}}^e = \mathbb{A}(t, \mathbb{X}^e), \quad (12)$$

where $\mathbb{A}(t, \mathbb{X}^e)$ stems from the evaluation of the right-hand side of either Eq.(5) or Eq.(6) and \mathbb{M}^e is the mass matrix of the element e .

Eventually, Eq.(12) is integrated in time using time-explicit Runge-Kutta algorithms, whose order match the order of the spatial discretization. Time-explicit integration schemes are conditionally stable and, as such, are subjected to the CFL condition [12]. Due to the presence of the damping terms σ_q^e in Eq.(6), the time-step restriction to be used in combination with the Runge-Kutta algorithms depends on whether Eq.(12) is derived from Eq.(5) or Eq.(6). In particular, if Eq.(12) stems from Eq.(5), the CFL condition reads

$$\frac{\tau}{h} < C \frac{f}{(1+2p)\lambda}, \quad (13)$$

whereas if Eq.(12) stems from Eq.(6), the CFL condition is

$$\frac{\tau}{h} < C \frac{f}{(1+2p)(\lambda + \sigma)}. \quad (14)$$

In Eqs.(13) and (14), τ denotes the maximum time step, f is the volume fraction threshold that triggers the cell merging, see [7, 16], C is a constant smaller than 1 that does not depend on the mesh size h or the order p of the basis functions, $\sigma \equiv \max_{e,q} \sigma_q^e$, and λ is the maximum wave speed on \mathcal{D} ; in inviscid gas dynamics, λ is $\lambda = \max_{\mathcal{D}}(\sqrt{v_k v_k} + a)$, where $\sqrt{v_k v_k}$ is the velocity magnitude and a is the speed of sound.

5. Results

Results are presented for two sets of tests, namely the supersonic vortex problem, see e.g. [19], and the embedded Sod's shock tube, see e.g. [7]. The former is a classic test in inviscid gas dynamics that is characterized by an analytical smooth solution and thus allows testing the high-order accuracy of numerical schemes. The latter reproduces a well-known mono-dimensional analytical solution of Eq.(1) characterized by a shock, a contact discontinuity and a rarefaction wave, in an inclined channel embedded in Cartesian grid, and thus allows testing the shock-capturing capabilities of the formulation for embedded geometries. In the remainder of this section, $\gamma = 1.4$ and all quantities are assumed non-dimensional.

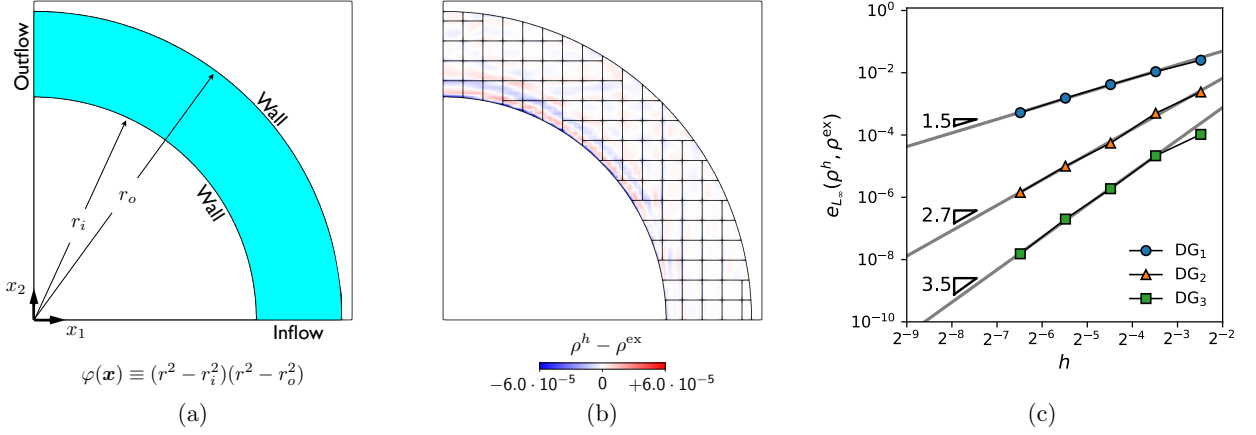


Figure 2 – (a) Geometry and boundary conditions of the supersonic vortex problem. (b) Error distribution obtained with a 16×16 background grid and a DG scheme with $p = 3$. (c) hp -convergence in the L_∞ norm of the density error.

The geometry and the boundary conditions of the supersonic vortex problem are sketched in Fig.(2a), where $r_i = 1$ and $r_o = 1.384$, and the geometry is embedded in a background square $\mathcal{R} \equiv [0, 1.43]^2$. The problem consists of an isentropic flow in the annular region and its exact solution is described by the fields

$$\rho^{\text{ex}} \equiv \rho_i \left[1 + \frac{\gamma-1}{2} M_i^2 \left(1 - \frac{r_i^2}{r^2} \right) \right]^{\frac{1}{\gamma-1}}, \quad \mathbf{v}^{\text{ex}} \equiv \begin{pmatrix} -\sin \theta \\ +\cos \theta \end{pmatrix} v_\theta \quad \text{and} \quad p^{\text{ex}} = (\rho^{\text{ex}})^\gamma / \gamma, \quad (15)$$

where $v_\theta \equiv a_i M_i r_i / r$, $r^2 = x_1^2 + x_2^2$, and $\rho_i = 1$, $a_i = 1$ and $M_i = 2.25$.

This problem setup does not lead to discontinuities; therefore, Eq.(5) may be used. The domain is meshed according to the procedure described in Sec.(3) using a $n \times n$ background grid such that the characteristic mesh size is defined as $h = 1.43/n$. The exact solution is used as initial conditions for the discrete problem, which is evolved in time up to $T = 5$. The computed solution is compared with the exact solution given in Eq.(15) and the following error measure is introduced

$$e_{L_\infty}(\rho^h, \rho^{\text{ex}}) \equiv \frac{\|\rho^h - \rho^{\text{ex}}\|_\infty}{\|\rho^{\text{ex}}\|_\infty}, \quad (16)$$

where $\|\cdot\|_\infty$ is the L_∞ norm defined over \mathcal{D}^h (by considering the maximum value among the quadrature points) and ρ^h denotes the density field computed using the present DG formulation. Figure (2b) shows the error in the density field when a 16×16 background grid and a DG scheme with $p = 3$ are employed. By changing the polynomial order and the grid resolution, one obtains the hp -convergence plot reported in Fig.(2c), which confirms the high-order accuracy of the scheme.

The geometry and the boundary conditions of the embedded Sod's shock tube problem are sketched in Fig.(3a), where $2r = 0.25$, $c = (1/2, 1/2)$ and the geometry is embedded in a background square $\mathcal{R} \equiv [0, 1]^2$. The orientation of the geometry is determined by the angle θ , which allows introducing the rotated coordinate system $\hat{\xi}\hat{\eta}$ whose unit vectors have components $\hat{\xi} = (\cos \theta, \sin \theta)$ and $\hat{\eta} = (-\sin \theta, \cos \theta)$. This facilitates the definition of the geometry via the level set function $\varphi = \eta^2 - r^2$

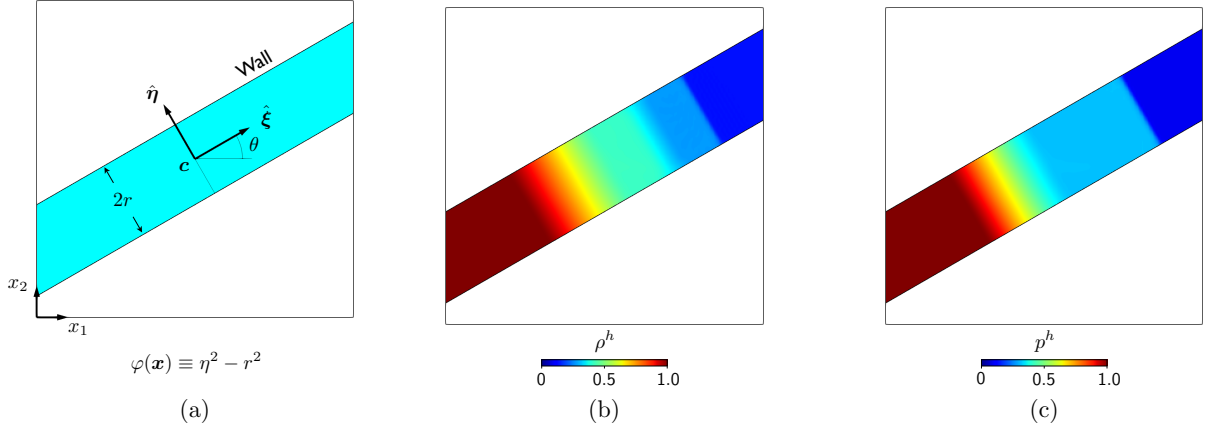


Figure 3 – (a) Geometry and boundary conditions of the embedded shock Sod's tube problem. (b) Density and (c) pressure distribution for $\theta = 30^\circ$ at the final time $t = 0.2$ computed using a 64×64 background grid and a DG scheme with $p = 2$.

where ξ and η are the components of \mathbf{x} in the rotated reference system. The initial conditions of the embedded Sod's shock tube problem are given by

$$U_0 = \begin{cases} U_L & \text{if } (x_k - c_k) \hat{\xi}_k \leq 0 \\ U_R & \text{if } (x_k - c_k) \hat{\xi}_k > 0 \end{cases} \quad \text{where} \quad U_L = \begin{pmatrix} 1 \\ \mathbf{0} \\ 1/(\gamma-1) \end{pmatrix} \quad \text{and} \quad U_R = \begin{pmatrix} 0.125 \\ \mathbf{0} \\ 0.1/(\gamma-1) \end{pmatrix}, \quad (17)$$

and the solution is evolved until $T = 0.2$.

In the rotated reference system, the solution of the considered problem is simply the solution of the mono-dimensional Riemann problem [20] between the two adjacent states defined in the initial conditions. More specifically, the analytical solution consists of a rarefaction wave, a contact discontinuity and a shock wave propagating normal to the tube's centerline. Figures (3b) and (3c) show the distribution of the density and the pressure fields, respectively, computed at the final time T using using a 64×64 background grid and a DG scheme with $p = 2$. As shown in the figure, the mono-dimensional character of the solution and the related waves, including the shock, are well-captured by the present formulation.

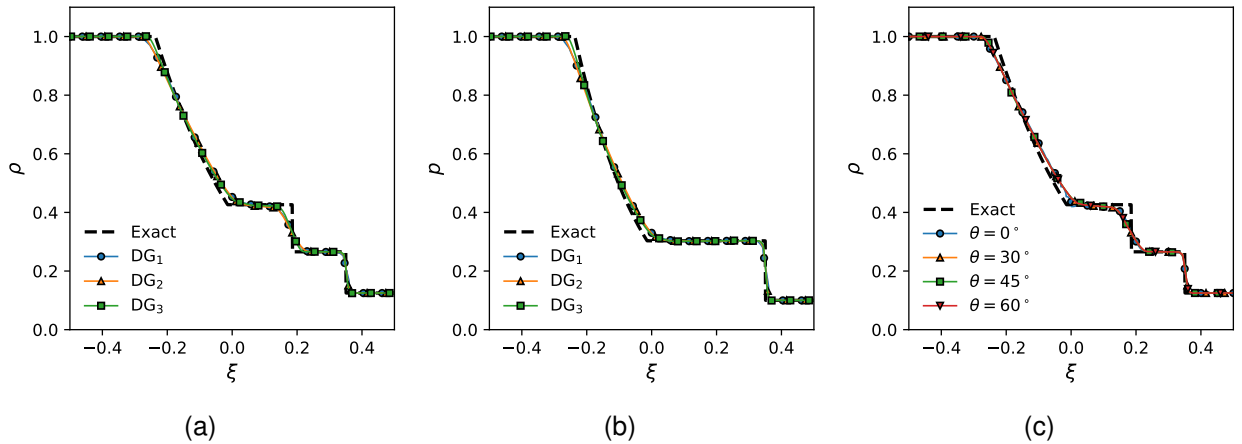


Figure 4 – Distribution of (a) density and (b) pressure along the embedded tube as functions of the employed DG scheme for $\theta = 30^\circ$. (c) Distribution of the density along the embedded tube as a function of the tube orientation computed using a DG scheme with $p = 2$.

The wave structure is clearer in Fig.(4), which displays the distribution of the density and the pressure fields along the centerline of the tube. In particular, Figs.(4a) and (4b) show the comparison between the exact solution and the computed values of the density field and pressure field, respectively, using different DG schemes; from the figures, it is possible to notice that, even though the damping

terms introduce some expected dissipation, all the considered DG schemes are able to reproduce the analytical solution with the DG₃ scheme featuring the least amount of dissipation. Eventually, Fig.(4a) shows the distribution of the density field as a function of the angle θ and demonstrates the robustness of the present formulation.

6. Conclusions

A novel formulation for solving the problem of inviscid gas-dynamics over embedded geometries has been presented. The formulation is based on discontinuous Galerkin schemes, which enable a high-order accurate solution of the governing equations in the regions of smooth flow, and on the use of suitably-defined damping terms, which allow resolving the presence of solution discontinuities without introducing non-physical oscillations that are typical of high-order methods for first-order hyperbolic PDEs. The formulation is also high-order accurate in time as it employs high-order Runge Kutta time-integration algorithms that match the order of the spatial discretization. Numerical tests have been performed on two-dimensional embedded geometries and have confirmed the high-order accuracy and the shock-capturing capabilities of the methodology. The proposed approach is currently being tested in combination with adaptive mesh refinement strategies and for three-dimensional problems, which will be presented in future studies.

7. Contact Author Email Address

mailto: vincenzo.gulizzi@unipa.it, vgulizzi@lbl.gov

8. Copyright Statement

The authors confirm that they, and/or their company or organization, hold copyright on all of the original material included in this paper. The authors also confirm that they have obtained permission, from the copyright holder of any third party material included in this paper, to publish it as part of their paper. The authors confirm that they give permission, or have obtained permission from the copyright holder of this paper, for the publication and distribution of this paper as part of the ICAS proceedings or as individual off-prints from the proceedings.

References

- [1] Aftosmis M, Berger M and Adomavicius G. A parallel multilevel method for adaptively refined Cartesian grids with embedded boundaries. *In 38th Aerospace Sciences Meeting and Exhibit*, Reno, NV, USA, pp 808, 2000.
- [2] Peskin CS. The immersed boundary method. *Acta numerica*, Vol. 11, pp 479-517, 2002.
- [3] Kemm F, Gaburro E, Thein F and Dumbser M. A simple diffuse interface approach for compressible flows around moving solids of arbitrary shape based on a reduced Baer-Nunziato model. *Computers & Fluids*, Vol. 204, p 104536, 2020.
- [4] Qin R, and Krivodonova L. A discontinuous Galerkin method for solutions of the Euler equations on Cartesian grids with embedded geometries. *Journal of Computational Science*, Vol. 4, No. 1-2, pp 24-35, 2013.
- [5] Saye R. Implicit mesh discontinuous Galerkin methods and interfacial gauge methods for high-order accurate interface dynamics, with applications to surface tension dynamics, rigid body fluid-structure interaction, and free surface flow: Part I. *Journal of Computational Physics*, Vol. 344 pp 647-682, 2017.
- [6] Saye R. Implicit mesh discontinuous Galerkin methods and interfacial gauge methods for high-order accurate interface dynamics, with applications to surface tension dynamics, rigid body fluid-structure interaction, and free surface flow: Part II. *Journal of Computational Physics* Vol. 344, pp 683-723, 2017.
- [7] Gulizzi V, Almgren AS and Bell JB. A coupled discontinuous Galerkin-Finite Volume framework for solving gas dynamics over embedded geometries. *Journal of Computational Physics*, Vol. 450, pp 110861, 2022.
- [8] Hartmann D, Meinke M and Schröder W. A strictly conservative Cartesian cut-cell method for compressible viscous flows on adaptive grids. *Computer Methods in Applied Mechanics and Engineering*, Vol. 200, No. 9-12, pp 1038-1052, 2011.
- [9] Cecere D and Giacomazzi E. An immersed volume method for large eddy simulation of compressible flows using a staggered-grid approach. *Computer Methods in Applied Mechanics and Engineering*, Vol. 280, pp 1-27, 2014.

- [10] Pember RB, Bell JB, Colella P, Curtchfield WY and Welcome ML. An adaptive Cartesian grid method for unsteady compressible flow in irregular regions. *Journal of computational Physics*, Vol. 120, No. 2, pp 278-304, 1995.
- [11] Berger M and Giuliani A. A state redistribution algorithm for finite volume schemes on cut cell meshes. *Journal of Computational Physics*, Vol. 428, p 109820, 2021.
- [12] Cockburn B and Shu CW. The Runge-Kutta discontinuous Galerkin method for conservation laws V: multidimensional systems. *Journal of Computational Physics*, Vol. 141, No. 2, pp 199-224, 1998.
- [13] Müller B, Krämer-Eis S, Kummer F and Oberlack M. A high-order discontinuous Galerkin method for compressible flows with immersed boundaries. *International Journal for Numerical Methods in Engineering*, Vol. 110, No. 1, pp 3-30, 2017.
- [14] Chaudhuri A, Jacobs GB, Don WS, Abbassi H, and Mashayek F. Explicit discontinuous spectral element method with entropy generation based artificial viscosity for shocked viscous flows. *Journal of Computational Physics*, Vol. 332, pp 99-117, 2017.
- [15] Geisenhofer M, Kummer F and Müller B. A discontinuous Galerkin immersed boundary solver for compressible flows: Adaptive local time stepping for artificial viscosity-based shock-capturing on cut cells. *International Journal for Numerical Methods in Fluids*, Vol. 91, No. 9, pp 448-472, 2019.
- [16] Gulizzi V and Saye R. Modeling wave propagation in elastic solids via high-order accurate implicit-mesh discontinuous Galerkin methods. *Computer Methods in Applied Mechanics and Engineering*, Vol. 395, pp 114971, 2022.
- [17] Lu J, Liu Y and Shu C-W. An oscillation-free discontinuous Galerkin method for scalar hyperbolic conservation laws. *SIAM Journal on Numerical Analysis*, Vol. 59, No. 3, pp 1299–1324, 2021.
- [18] Liu Y, Lu J, and Shu CW. An Essentially Oscillation-Free Discontinuous Galerkin Method for Hyperbolic Systems. *SIAM Journal on Scientific Computing*, Vol. 44, No. 1, pp A230-A259, 2022.
- [19] Krivodonova L, and Berger M. High-order accurate implementation of solid wall boundary conditions in curved geometries. *Journal of computational physics*, Vol. 211, No. 2, pp 492-512, 2006.
- [20] Toro EF. *Riemann solvers and numerical methods for fluid dynamics: a practical introduction*, Springer Science & Business Media, 2013.